ARTICLES
PUBLISHED ONLINE: 26 JUNE 2011 | DOI: 10.1038/NMAT3043
nature materials

Hybrid elastic solids

Yun Lai[1,2], Ying Wu[1,3], Ping Sheng[1] and Zhao-Qing Zhang[1]*

Metamaterials can exhibit electromagnetic and elastic characteristics beyond those found in nature. In this work, we present a design of elastic metamaterial that exhibits multiple resonances in its building blocks. Band structure calculations show two negative dispersion bands, of which one supports only compressional waves and thereby blurs the distinction between a fluid and a solid over a finite frequency regime, whereas the other displays 'super anisotropy' in which compressional waves and shear waves can propagate only along different directions. Such unusual characteristics, well explained by the effective medium theory, have no comparable analogue in conventional solids and may lead to novel applications.

Double-negative electromagnetic materials denote those artificial structures in which both the dielectric constant ε and magnetic permeability μ are simultaneously negative within a certain frequency regime. The initial proposal[1] and its more recent realizations[2–8] permit the index of refraction to take negative values, with broad scientific and practical implications[9–16]. The ability of double-negative metamaterials to possess unusual electromagnetic responses is bestowed by the special resonances provided by its unit structure. This principle is equally valid for acoustic and elastic materials. An acoustic metamaterial comprising locally resonant units[17] was shown to exhibit negative mass density[18,19]; and negative bulk modulus was demonstrated in a system of Helmholtz resonators[20]. By combining the two, various schemes have been proposed and implemented to realize a double-negative characteristic for the compressional wave[21–25], in analogy with the double-negative electromagnetic materials.

The ability to withstand shear is a trait that distinguishes a solid from a liquid. In an elastic solid, the increased number of relevant material parameters, when combined with the possibility of double negativity, can yield characteristics that are much more complex than those seen in electromagnetic and acoustic metamaterials, some of which, as we show here, can blur the delineating feature between a solid and a liquid within a certain frequency regime.

For a solid in a periodic structure, the dispersion is in general anisotropic. Even in the simplest case of a square lattice, one must take into consideration the realization of negative values for not only mass density ρ, but also three elastic moduli[26], namely c_{11}, c_{12} and c_{44}, as well as the various possible interactions between these parameters. Intriguing possibilities arise. For example, if both mass density and compressional wave moduli are negative within a certain frequency regime, then one may have only a negative band propagating compressional waves (and evanescent shear waves), which makes a solid 'fluid-like'. Another possibility is to have negative dispersions for the compressional wave and shear wave along distinct directions. The potential realization of such possibilities, or even a subset, would open new horizons in solid wave mechanics. Here we would like to mention that anisotropy in semiconductor superlattices can also give rise to some interesting phenomenon. It was shown that hybridization of longitudinal acoustic phonons and folded slow-transverse phonons can create a band gap inside the Brillouin zone in addition to those at the zone boundary and the zone centre[27].

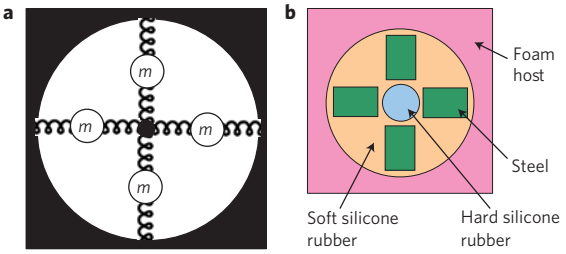

Figure 1 | Physical model and a practical design. a, The physical model of a type of multi-mass resonating unit cell that can support monopolar, dipolar and quadrupolar resonances, and lead to novel elastic properties. **b**, A realistic elastic metamaterial unit that is designed according to the physical model in **a**.

A unit cell with multiple resonances

We propose a type of two-dimensional elastic metamaterial with its unit cell comprising a multi-mass locally resonant inclusion that can generate resonances with monopolar, dipolar and quadrupolar characteristics. The proposed unit cell is shown to lead to negative values, not only for mass density, but also for certain elastic moduli. With physically realizable material parameters, we use finite element simulations to demonstrate that when these unit cells are arranged in a simple square lattice, there can be two hybridized bands with novel characteristics. One of the hybridized band lies in the double-negative frequency regime for mass density and compressional wave moduli, so that only longitudinal pressure waves can propagate (with negative dispersion), whereas transverse shear waves decay exponentially. In the other band it is found that along distinct directions only longitudinal pressure waves or transverse waves are allowed, both with negative dispersions. These phenomena, absent in nature, are denoted as 'fluid-like' and 'super-anisotropic', respectively.

A schematic figure of the physical model of the unit cell is shown in Fig. 1a. The model is a mass–spring system composed of four masses connected to each other and to the host by springs. Collective motion of the four masses can enhance the dipolar resonance (for negative mass density), whereas their relative motions can enhance the quadrupolar and monopolar resonances (for negative moduli). A practical realization of the model in Fig. 1a is illustrated in Fig. 1b. The resonant inclusions

[1]Department of Physics, Hong Kong University of Science and Technology, Clear Water Bay, Kowloon, Hong Kong, China, [2]Department of Physics, Soochow University, 1 Shizi Street, Suzhou 215006, China, [3]Division of Mathematical and Computer Sciences and Engineering, King Abdullah University of Science and Technology, Thuwal 23955-6900, Kingdom of Saudi Arabia. *e-mail: phzzhang@ust.hk.

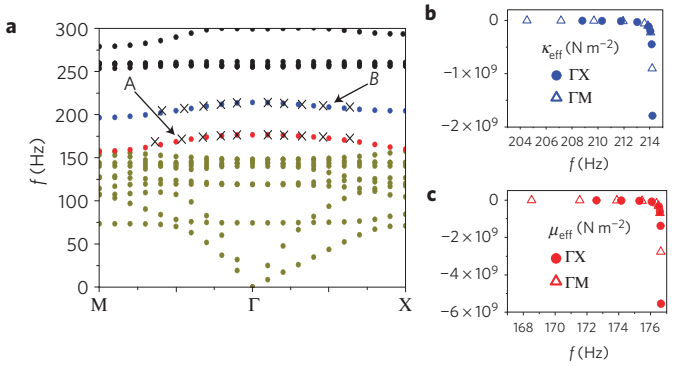

Figure 2 | Band structure and effective medium parameters. a, The band structure of the elastic metamaterial. Two distinct negative bands are marked by red and blue dots, respectively. The crosses indicate the dispersions obtained by using the effective medium theory. **b**, The κ^{eff} for the higher frequency negative band, exhibiting large negative values at the upper band edge, that is, close to the Γ point. **c**, The μ^{eff} for the lower frequency negative band, exhibiting large negative values at the upper band edge, that is, close to the Γ point.

are composed of a soft silicone rubber rod embedded with a hard silicone rubber rod, surrounded by four rectangular steel rods. The matrix material is chosen to be a foam that has a light mass density as well as low moduli. The square lattice has a lattice constant of 10 cm; the radii of the soft and hard silicone rubber rods are 4 cm and 1 cm, respectively; the rectangular steel rods are 1.6 cm × 2.4 cm in size, located at a distance of 2.4 cm from the centre. The material parameters are taken to be $\rho = 115\,\text{kg m}^{-3}$, $\lambda = 6 \times 10^6\,\text{N m}^{-2}$, $\mu = 3 \times 10^6\,\text{N m}^{-2}$ for foam[28]; $\rho = 1.3 \times 10^3\,\text{kg m}^{-3}$, $\lambda = 6 \times 10^5\,\text{N m}^{-2}$, $\mu = 4 \times 10^4\,\text{N m}^{-2}$ for soft silicone rubber[17]; $\rho = 1.415 \times 10^3\,\text{kg m}^{-3}$, $\lambda = 1.27 \times 10^9\,\text{N m}^{-2}$, $\mu = 1.78 \times 10^6\,\text{N m}^{-2}$ for hard silicone rubber (J. Page, personal communication); $\rho = 7.9 \times 10^3\,\text{kg m}^{-3}$, $\lambda = 1.11 \times 10^{11}\,\text{N m}^{-2}$, $\mu = 8.28 \times 10^{10}\,\text{N m}^{-2}$ for steel. At certain frequencies, the four rectangular steel rods serve as the four masses, while the silicone rubber rods serve as the springs in Fig. 1a. The insertion of the hard silicone rubber is for the purpose of adjusting the spring constants between the masses.

Band structure and eigenstates

The band structure of the elastic composite in Fig. 1b was calculated by using a finite element solver (COMSOL Multiphysics) and is shown in Fig. 2a. There are two bands (red and blue dots) with negative curvatures. The lower frequency negative dispersion band (red dots) has a bandwidth of about 18 Hz. A small complete gap (178 Hz–198 Hz) separates it from a higher frequency negative dispersion band (blue dots) which has a bandwidth of about 18 Hz along the ΓM direction but only 10 Hz in the ΓX direction. There is also a complete gap above the higher negative band (216 Hz–255 Hz). We note that, around 200 Hz, the transverse and longitudinal wavelengths in the foam host are, respectively, about 80 cm and 160 cm; much larger than the lattice constant of 10 cm. Thus, these negative bands are not induced by Bragg scattering but are rather the results of hybridization between different types of resonances within the unit cell.

An investigation of the eigenstates in the bands gives us a clear picture of the physical origin of the bands. The eigenstates in the low-frequency bands, delineated in Fig. 2a by dark yellow, red and blue dots, have their kinetic energy (both vibrational and rotational) mostly concentrated in the steel rods. In contrast, for eigenstates in the high-frequency bands, delineated in Fig. 2a by black dots, the energy is mostly concentrated inside the soft silicone rubber. The origin of the band gaps shown in Fig. 2a is the collective motions

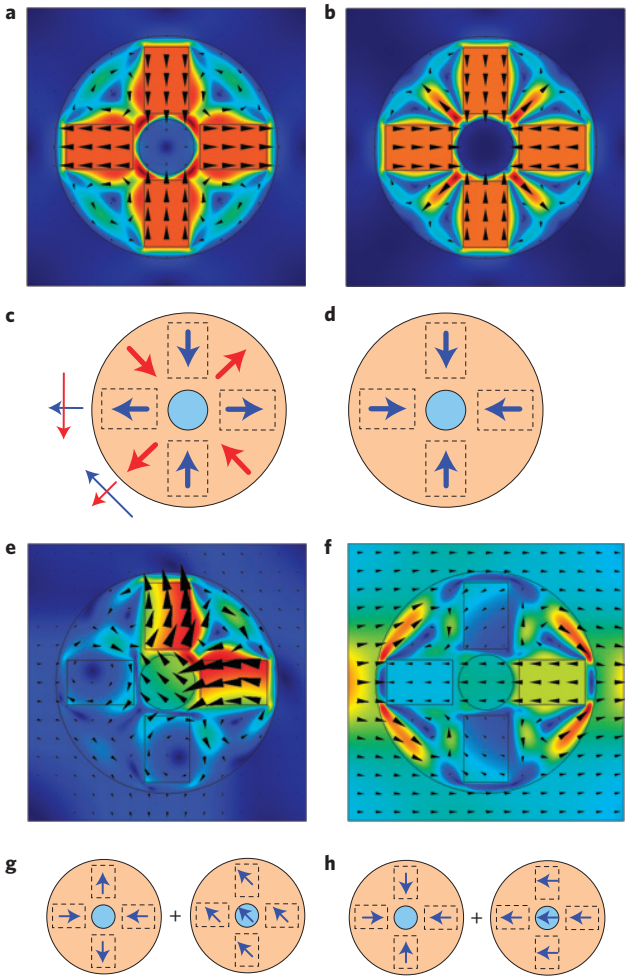

Figure 3 | Field distributions of some specific eigenstates. a,**b**, The eigenstates ($f = 178.5$ Hz and 216.8 Hz) at the Γ point in the lower and upper negative bands, respectively. Here, arrows indicate displacements and colour indicates amplitude (red for large and blue for small). **c**,**d**, The displacements of the quadrupolar and monopolar resonances that correspond to **a** and **b**, respectively. **e**, The eigenstate ($f = 169.4$ Hz) at the midpoint between the Γ and M points in the lower negative band (marked by A in Fig. 2a). **f**, The eigenstate ($f = 210.3$ Hz) at the midpoint between the Γ and X points in the upper negative band (marked by B in Fig. 2a). **g**,**h**, The states in **e** and **f** are shown to arise as hybridizations, (quadrupole + dipole) and (monopole + dipole), respectively.

of steel rods that enhance dipolar resonances and thus produces a negative mass density within the frequency range of 160 Hz–255 Hz, in a manner similar to single-mass resonator metamaterials[17]. However, as well as the dipolar resonance, the relative motions of steel rods can support two other important resonances, namely, the monopolar and quadrupolar resonances, which are found to be responsible for the two negative bands (blue and red dots) inside the range of negative mass density. In Fig. 3a and b, we plot the two eigenstates in the lower and upper negative bands ($f = 178.5$ Hz and 216.8 Hz) at the Γ point, respectively. Here, the colour represents the amplitude of displacement (blue/red for small/large values) and the arrows show the displacement vectors directly. The eigenstate in Fig. 3a is clearly a quadrupolar resonance, whereas the eigenstate in Fig. 3b is a monopolar resonance. Schematics of the two resonances are shown by the blue thick arrows in Fig. 3c and d, respectively, which indicate the displacements in the positions of the steel rods and exhibit clear quadrupolar and monopolar signatures. Thus, we can view the two negative bands as being

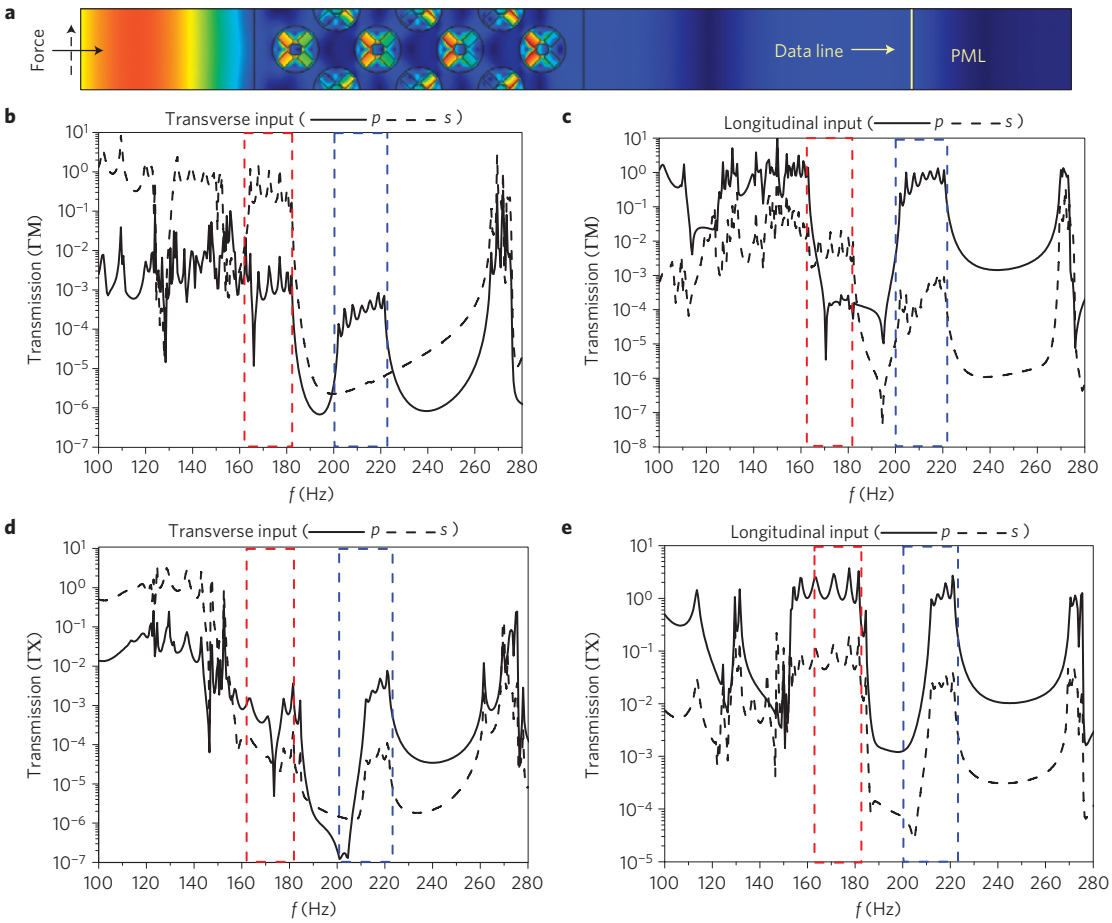

Figure 4 | Transmission through a finite sample. a, The numerical set-up for transmission computations. **b**,**c**, Transmission along the ΓM direction for transverse input excitations (**b**) and longitudinal input excitations (**c**). Transmission along the ΓX direction for transverse input excitations (**d**) and longitudinal input excitations (**e**). In the upper frequency negative dispersion band, indicated by the blue dashed lines, it is seen that whereas longitudinal excitations can lead to large transmissions along both the ΓM and ΓX directions (**c**,**e**), strong attenuation is seen for transverse input excitations (**b**,**d**). For the lower frequency negative dispersion band, indicated by the red dashed lines, large transmissions are seen in **b** and **e**, in exact agreement with the effective medium predictions.

induced by quadrupolar and monopolar resonances inside the band gap created by the dipolar resonance. This may be viewed as the hybridization effect of the quadrupolar/monopolar resonance with the dipolar resonance.

To directly see the hybridization effect, we plot in Fig. 3e and f the state at the midpoint between the Γ and M points in the lower negative band (marked by the symbol 'A' with $f = 169.4$ Hz) and the state at the midpoint between the Γ and X points in the upper negative band (marked by the symbol 'B' with $f = 210.3$ Hz), respectively. It is seen that away from the Γ point, the pure quadrupolar or monopolar states turn into hybrid states that can be regarded as combinations of a monopolar or quadrupolar state and a dipolar state. These are illustrated in Fig. 3g and h, respectively. These hybrid states have negative non-zero group velocities and thus can transmit energy.

Effective medium description

The formation of negative bands can be understood from an effective medium point of view. It is known that dipolar resonances can lead to negative mass density[17–19], whereas monopolar and quadrupolar resonances are associated with certain elastic moduli[28,29]. From the theory of linear elasticity, the three elastic moduli for a solid with a square lattice are c_{11}, c_{12} and c_{44}. The dispersions and the associated modes can be obtained from the Christoffel's equation[26]. Along the ΓX direction, compressional wave and shear wave velocities are given by $\sqrt{c_{11}/\rho}$ and $\sqrt{c_{44}/\rho}$, respectively; whereas along the ΓM direction the compressional and shear wave velocities are $\sqrt{(c_{11}+c_{12}+2c_{44})/(2\rho)}$ and $\sqrt{(c_{11}-c_{12})/(2\rho)}$, respectively. Thus, we can predict the transport properties of this hybrid elastic solid if we can obtain the effective medium parameters. Owing to the strongly anisotropic nature of the relative motions that are possible within our unit cell, an effective medium theory that relies on the surface motion/response to external stimuli (in contrast to volume average), is shown to be more generally applicable to calculate the effective parameters along both ΓX and ΓM directions.

Along the ΓX and ΓM directions, we find that it is convenient to introduce $\kappa^{\mathrm{eff}} = (c_{11}^{\mathrm{eff}} + c_{12}^{\mathrm{eff}})/2$ and $\mu^{\mathrm{eff}} = (c_{11}^{\mathrm{eff}} - c_{12}^{\mathrm{eff}})/2$ as the effective elastic bulk modulus and shear modulus that correspond with the monopolar and quadrupolar resonances, respectively. Whereas $\rho^{\mathrm{eff}} = -F_x^{\mathrm{eff}}/\omega^2 u_x^{\mathrm{eff}} a^2$, where both the effective force F_x^{eff} on the unit cell and its effective displacement u_x^{eff} may be obtained from surface integration of the stresses (along the x direction) and the displacements over the unit cell, the effective moduli are evaluated from the effective stress and strain relations: $T_{xx}^{\mathrm{eff}} = c_{11}^{\mathrm{eff}} S_{xx}^{\mathrm{eff}} + c_{12}^{\mathrm{eff}} S_{yy}^{\mathrm{eff}}$, $T_{yy}^{\mathrm{eff}} = c_{12}^{\mathrm{eff}} S_{xx}^{\mathrm{eff}} + c_{11}^{\mathrm{eff}} S_{yy}^{\mathrm{eff}}$, and $T_{xy}^{\mathrm{eff}} = 2c_{44}^{\mathrm{eff}} S_{xy}^{\mathrm{eff}}$, where both the effective stresses and the effective strains are evaluated on the unit cell boundary. Details can be found in the Supplementary Information.

In the lower negative band, the μ^{eff} evaluated from the relevant eigenstates is negative and diverges (in the negative direction) at the Γ point owing to the quadrupolar resonance, whereas κ^{eff} is

positive and finite. In the higher negative band, κ^{eff} is negative and diverges (in the negative direction) at the Γ point owing to the monopolar resonance, whereas μ^{eff} is positive and finite. The compressional wave and shear wave velocities along the ΓX (ΓM) direction can be obtained by $\sqrt{(\kappa^{\text{eff}}+\mu^{\text{eff}})/\rho^{\text{eff}}}$ ($\sqrt{(\kappa^{\text{eff}}+c_{44}^{\text{eff}})/\rho^{\text{eff}}}$) and $\sqrt{c_{44}^{\text{eff}}/\rho^{\text{eff}}}$ ($\sqrt{\mu^{\text{eff}}/\rho^{\text{eff}}}$), respectively. From these formulas, it can be clearly seen that in the higher frequency negative dispersion band, the fact that $\kappa^{\text{eff}} \ll 0$, $\rho^{\text{eff}} < 0$, $\mu^{\text{eff}} > 0$ and $c_{44}^{\text{eff}} > 0$ implies only the longitudinal wave can propagate along the ΓX and ΓM directions. For the lower frequency negative dispersion band we have $\mu^{\text{eff}} \ll 0$, $\rho^{\text{eff}} < 0$ and other parameters positive, therefore only the longitudinal (transverse) wave can propagate along the ΓX (ΓM) direction. The resulting effective medium predictions of the dispersion relations are shown as crosses in Fig. 2a. The agreement is excellent. It should be noted, however, that owing to the nature of quadrupolar excitation, c_{44}^{eff} for the lower negative band cannot be obtained from the effective medium theory. Thus the condition $c_{44}^{\text{eff}} > 0$ is inferred by consistency with the band structures.

Discussion of novel characteristics

The above effective medium analysis predicts that this solid metamaterial has very unusual acoustic properties, beyond those of normal solids. In the higher frequency negative dispersion band, the elastic metamaterial can only transport pressure waves and thus turns 'fluid-like'. Therefore, its impedance can be perfectly matched to a fluid host or soft tissues where pressure waves dominate. In the lower frequency negative dispersion band, the metamaterial turns into a very unique anisotropic solid that is 'fluid-like' in certain directions and 'incompressible-solid-like' (that is, allowing only shear waves) in certain other directions, a property which is denoted 'super-anisotropic'. In the following, we perform transmission calculations by using COMSOL Multiphysics to illustrate the transmission properties of the hybrid bands. A schematic for the numerical set-up in COMSOL is shown in Fig. 4a. For a slab of metamaterial with seven layers along the ΓM direction, an external normal/tangential harmonic force is exerted on the left side to provide an input of longitudinal/transverse waves. A perfect matched layer (PML) is added at the right side and periodic boundary conditions are imposed on the upper and lower edges. The transmissions for the longitudinal or transverse waves (denoted as '*p*' or '*s*') can be calculated by integrating the horizontal or vertical displacements on the data line. In Fig. 4b,c, we show the obtained transmissions in the ΓM direction under transverse and longitudinal inputs, respectively. It is seen that large transmissions (on the order of one) for *p* waves are obtained for the upper negative dispersion band (delineated by blue dashed lines) under a longitudinal input. By contrast, large transmissions for *s* waves are obtained for the lower negative dispersion band (delineated by red dashed lines) under a transverse input. In Fig. 4d,e, we show the obtained transmissions along the ΓX direction under transverse and longitudinal inputs, respectively. Large transmissions are seen only for longitudinal input excitations, for both negative dispersion bands. The results are in exact agreement with the predictions of the effective medium theory. Here we note that there are some transmission values greater than one in Fig. 4b–e caused by the use of force (load) as input instead of incident waves, but these (normalization issues) do not affect the analysis here.

The 'super-anisotropic' behaviour can be understood as a result of symmetry breaking in the rubber rod due to the presence of four steel rods. As shown in Fig. 3c, a local quadrupolar resonance in a cylindrically symmetric rubber rod (without the steel rods) has two degenerate modes at the Γ point (with displacements marked as red and blue thick arrows). By matching with the displacements of the host medium (red and blue thin arrows), it is seen that one mode (red arrows) is transverse in the ΓX direction and longitudinal in the ΓM direction, whereas the other mode (blue arrows) is just the opposite. When the steel rods are inserted at the positions of the dashed boxes, the symmetry of the rubber rod is broken and the two degenerate states split. The one denoted by blue arrows in Fig. 3c leads to the lower negative band with the 'super-anisotropic' elastic characteristic shown in Fig. 2a.

We note that, in general, the theory of linear elasticity needs to be modified so as to accommodate the finite-size limitation of the unit cell in elastic metamaterials[30–32]. During the effective medium calculation of the lower negative band, we have actually observed stresses $T_{xy}^{\text{eff}} \neq T_{yx}^{\text{eff}}$, which implies 'local rotations' beyond the linear elastic theory. However, this 'local rotation' effect does not have a major impact on the phenomena shown in this paper, as they are actually determined by the resonances involving the diagonal terms, namely T_{xx}^{eff} and T_{yy}^{eff}, as can be seen from the divergence of κ^{eff} and μ^{eff} in Fig. 2b and c, respectively. Nevertheless, the 'local rotation' effect may have some interesting implications in other types of metamaterials[30–32].

The 'fluid-like' and 'super-anisotropic' hybrid elastic solids shown in this report represent two types of new solids absent in nature. They significantly extend our ability to control elastic waves in solids. Potential applications of these hybrid elastic solids include wave polarizers, wave imaging and confinement[33], controlling elastic and seismic waves[34,35], transformation acoustics[36], and so on. As a result of their double-negative nature, negative refraction and superlensing for longitudinal or transverse components are also possible. Having a richer variety of unusual properties than their electromagnetic and acoustic counterparts, elastic metamaterials are likely to generate further new ideas and novel applications in the near future.

Received 17 January 2011; accepted 6 May 2011; published online 26 June 2011

References

1. Pendry, J. B., Holden, A. J., Robbins, D. J. & Stewart, W. J. Magnetism from conductors and enhanced nonlinear phenomena. *IEEE Trans. Microwave Theory Tech.* **47,** 2075–2084 (1999).
2. Shelby, R. A., Smith, D. R. & Schultz, S. Experimental verification of a negative index of refraction. *Science* **292,** 77–79 (2001).
3. Smith, D. R., Pendry, J. B. & Wiltshire, M. C. K. Metamaterials and negative refractive index. *Science* **305,** 788–792 (2004).
4. Fang, N., Lee, H., Sun, C. & Zhang, X. Sub-diffraction-limited optical imaging with a silver superlens. *Science* **308,** 534–537 (2005).
5. Soukoulis, C. M., Linden, S. & Wegener, M. Negative refractive index at optical wavelengths. *Science* **315,** 47–49 (2007).
6. Lezec, H. J., Dionne, J. A. & Atwater, H. A. Negative refraction at visible frequencies. *Science* **316,** 430–432 (2007).
7. Valentine, J. *et al.* Three-dimensional optical metamaterial with a negative refractive index. *Nature* **455,** 376–379 (2008).
8. Yao, J. *et al.* Optical negative refraction in bulk metamaterials of nanowires. *Science* **321,** 930 (2008).
9. Veselago, V. G. The electrodynamics of substances with simultaneously negative values of ε and μ. *Sov. Phys. Usp.* **10,** 509–514 (1968).
10. Pendry, J. B. Negative refraction makes a perfect lens. *Phys. Rev. Lett.* **85,** 3966–3969 (2000).
11. Leonhardt, U. Optical conformal mapping. *Science* **312,** 1777–1780 (2006).
12. Pendry, J. B., Schurig, D. & Smith, D. R. Controlling electromagnetic fields. *Science* **312,** 1780–1782 (2006).
13. Pendry, J. B. & Ramakrishna, S. A. Near-field lenses in two dimensions. *J. Phys. Condens. Matter* **14,** 8463–8479 (2002).
14. Yang, T., Chen, H. Y., Luo, X. D. & Ma, H. R. Superscatterer: Enhancement of scattering with complementary media. *Opt. Express* **16,** 18545–18550 (2008).
15. Lai, Y., Chen, H. Y., Zhang, Z. Q. & Chan, C. T. Complementary media invisibility cloak that cloaks objects at a distance outside the cloaking shell. *Phys. Rev. Lett.* **102,** 093901 (2009).
16. Lai, Y. *et al.* Illusion optics: The optical transformation of an object into another object. *Phys. Rev. Lett.* **102,** 253902 (2009).
17. Liu, Z. *et al.* Locally resonant sonic materials. *Science* **289,** 1734–1736 (2000).
18. Liu, Z., Chan, C. T. & Sheng, P. Analytic model of phononic crystals with local resonances. *Phys. Rev. B* **71,** 014103 (2005).
19. Yang, Z., Mei, J., Yang, M., Chan, N. H. & Sheng, P. Membrane-type acoustic metamaterial with negative dynamic mass. *Phys. Rev. Lett.* **101,** 204301 (2008).
20. Fang, N. *et al.* Ultrasonic metamaterials with negative modulus. *Nature Mater.* **5,** 452–456 (2006).

21. Ding, Y. Q., Liu, Z. Y., Qiu, C. Y. & Shi, J. Metamaterial with simultaneously negative bulk modulus and mass density. *Phys. Rev. Lett.* **99,** 093904 (2007).
22. Li, J. & Chan, C. T. Double-negative acoustic metamaterial. *Phys. Rev. E* **70,** 055602 (2004).
23. Lee, S. H., Park, C. M., Seo, Y. M., Wang, Z. G. & Kim, C. K. Composite acoustic medium with simultaneously negative density and modulus. *Phys. Rev. Lett.* **104,** 054301 (2010).
24. Li, J., Fok, L., Yin, X. B., Bartal, G. & Zhang, X. Experimental demonstration of an acoustic magnifying hyperlens. *Nature Mater.* **8,** 931–934 (2009).
25. Zhang, S., Yin, L. L. & Fang, N. Focusing ultrasound with an acoustic metamaterial network. *Phys. Rev. Lett.* **102,** 194301 (2009).
26. Royer, D. & Dieulesaint, E. *Elastic Waves in Solids* (Springer, 1999).
27. Tamura, S & Wolfe, J. P. Coupled-mode stop bands of acoustic phonons in semiconductor superlattices. *Phys. Rev. B* **35,** 2528–2531 (1987).
28. Zhou, X. M. & Hu, G. K. Analytic model of elastic metamaterials with local resonances. *Phys. Rev. B* **79,** 195109 (2009).
29. Wu, Y., Lai, Y. & Zhang, Z. Q. Effective medium theory for elastic metamaterials in two dimensions. *Phys. Rev. B* **76,** 205313 (2007).
30. Milton, G. W. New metamaterials with macroscopic behaviour outside that of continuum elastodynamics. *New J. Phys.* **9,** 359 (2007).
31. Milton, G. W. & Willis, J. R. On modifications of Newton's second law and linear continuum elastodynamics. *Proc. R. Soc. A* **463,** 855–880 (2007).
32. Willis, J. R. The nonlocal influence of density variations in a composite. *Int. J. Solids Struct.* **210,** 805–817 (1985).
33. Guenneau, S., Movchan, A., Petursson, G. & Ramakrishna, S. A. Acoustic metamaterials for sound focusing and confinement. *New J. Phys.* **9,** 399 (2007).
34. Brun, M., Guenneau, S. & Movchan, A. B. Achieving control of in-plane elastic waves. *Appl. Phys. Lett.* **94,** 061903 (2009).
35. Farhat, M., Guenneau, S. & Enoch, S. Ultrabroadband elastic cloaking in thin plates. *Phys. Rev. Lett.* **103,** 024301 (2009).
36. Chen, H. Y. & Chan, C. T. Acoustic cloaking and transformation acoustics. *J. Phys. D* **43,** 113001 (2010).

Acknowledgements

We thank Z. Hang and I. Tsukerman for useful discussions. This work was supported by Hong Kong RGC Grant No. 605008 and RGC Grant HKUST604207.

Author contributions

Y.L. and Y.W. carried out the research and contributed equally. P.S. and Z-Q.Z. supervised the research and contributed to its design. All the authors discussed the results extensively.

Additional information

The authors declare no competing financial interests. Supplementary information accompanies this paper on www.nature.com/naturematerials. Reprints and permissions information is available online at http://www.nature.com/reprints. Correspondence and requests for materials should be addressed to Z-Q.Z.

nature materials

SUPPLEMENTARY INFORMATION

DOI: 10.1038/NMAT3043

Hybrid Elastic Solids

Yun Lai, Ying Wu, Ping Sheng, Zhao-Qing Zhang*

Department of Physics, Hong Kong University of Science and Technology

Clear Water Bay, Kowloon, Hong Kong, China

E-mail: phzzhang@ust.hk

DOI: 10.1038/NMAT3043

1. Describing our system using Christoffel's equation

Our system is a two-dimensional elastic solid in a square lattice, and we consider only elastic waves with displacements in the *x*-*y* plane. Due to the high symmetry, the stiffness tensor is greatly simplified such that only c_{11} , c_{12} and c_{44} exist, and the constitutive relation takes the simple form as

$$\begin{pmatrix} T_{xx} \\ T_{yy} \\ T_{xy} \end{pmatrix} = \begin{pmatrix} c_{11} & c_{12} & 0 \\ c_{12} & c_{11} & 0 \\ 0 & 0 & c_{44} \end{pmatrix} \cdot \begin{pmatrix} S_{xx} \\ S_{yy} \\ 2S_{xy} \end{pmatrix}, \tag{S1}$$

where T_{ij} is the stress tensor and $S_{ij} = \frac{1}{2}\left(\frac{\partial u_i}{\partial x_j} + \frac{\partial u_j}{\partial x_i} \right)$ is the strain tensor and u_i is the displacement in the *i*th direction. By substituting Eq. S1 into the Newton's second law, i.e. $\rho \partial^2 u_i / \partial t^2 = \partial T_{ij} / \partial x_j$ where ρ is mass density, and using a plane wave solution of the form $u_i = u_i^0 F\left(t - (\mathbf{n}\cdot\mathbf{x})/v\right)$, where v is phase velocity, u_i^0 denote the wave polarization vector, and n_i denote the propagation direction, we find the following equations of in-plane elastic waves (*S1*), i.e.,

$$\rho v^2 \begin{pmatrix} u_x^0 \\ u_y^0 \end{pmatrix} = \begin{pmatrix} c_{11}\cos^2\varphi + c_{44}\sin^2\varphi & (c_{12}+c_{44})\sin\varphi\cos\varphi \\ (c_{12}+c_{44})\sin\varphi\cos\varphi & c_{11}\sin^2\varphi + c_{44}\cos^2\varphi \end{pmatrix} \cdot \begin{pmatrix} u_x^0 \\ u_y^0 \end{pmatrix}. \tag{S2}$$

By solving the secular equation of Eq. S2, we obtain two eigenvalues, i.e., phase velocities as functions of the angle φ ($n_1 = \cos\varphi$, $n_2 = \sin\varphi$)

$$\begin{aligned} 2\rho v_1^2 &= c_{11} + c_{44} + \sqrt{(c_{11}-c_{44})^2 \cos^2 2\varphi + (c_{12}+c_{44})^2 \sin^2 2\varphi}, \\ 2\rho v_2^2 &= c_{11} + c_{44} - \sqrt{(c_{11}-c_{44})^2 \cos^2 2\varphi + (c_{12}+c_{44})^2 \sin^2 2\varphi}. \end{aligned} \tag{S3}$$

The corresponding eigenvectors give the polarizations of the plane waves, which can be obtained from the two orthogonal solutions of the equation $\tan 2\beta = \frac{(c_{12}+c_{44})}{(c_{11}-c_{44})} \tan 2\varphi$, with β defining the polarization through $\tan\beta = \frac{u_y^0}{u_x^0}$ (Ref. *S1*). In general, the polarization is neither longitudinal nor transverse. However, for $\varphi = 0$, $v_1 = \sqrt{(c_{11}/\rho)}$ is the velocity of a pure longitudinal wave and $v_2 = \sqrt{(c_{44}/\rho)}$ is the velocity of a pure transverse wave. For $\varphi = \pi/4$, the velocity $v_1 = \sqrt{(c_{11}+c_{12}+2c_{44})/2\rho}$ refers to a pure longitudinal wave and the velocity $v_2 = \sqrt{(c_{11}-c_{12})/2\rho}$ refers to a pure transverse wave.

If we define the parameters $\kappa = (c_{11} + c_{12})/2$ and $\mu = (c_{11} - c_{12})/2$, then we can rewrite the velocities as $v_1 = \sqrt{(\kappa + \mu)/\rho}$ for longitudinal waves and $v_2 = \sqrt{c_{44}/\rho}$ for transverse waves in the case of $\varphi = 0$; $v_1 = \sqrt{(\kappa + c_{44})/\rho}$ for longitudinal waves and $v_2 = \sqrt{\mu/\rho}$ for transverse waves in the case of $\varphi = \pi/4$.

Simple analysis:

Consider the case when $\rho < 0$, $\kappa \ll 0$, $\mu > 0$ and $c_{44} > 0$, which happens near the resonant frequency of κ in a band gap induced by $\rho < 0$, as for the higher negative band in our paper. For $\varphi = 0$, we find $\kappa + \mu < 0$, thus $v_1 = \sqrt{(\kappa + \mu)/\rho}$ is real and $v_2 = \sqrt{c_{44}/\rho}$ is imaginary. Thus only longitudinal waves are allowed. For $\varphi = \pi/4$, we find $\kappa + c_{44} < 0$, thus $v_1 = \sqrt{(\kappa + c_{44})/\rho}$ is real and $v_2 = \sqrt{\mu/\rho}$ is imaginary. Thus only longitudinal waves are allowed too. For other directions, if we consider $|\kappa|$ is much larger than other parameters, then we find $v_1 \approx \sqrt{\kappa/\rho}$ and $\beta \approx \varphi$. This indicates almost pure longitudinal waves in any direction.

Consider the case when $\rho < 0$, $\kappa > 0$, $\mu \ll 0$ and $c_{44} > 0$, which happens near the resonant frequency of μ in a band gap induced by $\rho < 0$, as the lower negative band in our paper. For $\varphi = 0$, we find $\kappa + \mu < 0$, thus $v_1 = \sqrt{(\kappa + \mu)/\rho}$ is real and $v_2 = \sqrt{c_{44}/\rho}$ is imaginary. Thus only longitudinal waves are allowed. For $\varphi = \pi/4$, we find $v_1 = \sqrt{(\kappa + c_{44})/\rho}$ is imaginary and $v_2 = \sqrt{\mu/\rho}$ is real. Thus only transverse waves are allowed instead. For other directions, the polarization is neither pure transverse or pure longitudinal, but a mixed type.

DOI: 10.1038/NMAT3043

2. The boundary effective medium theory

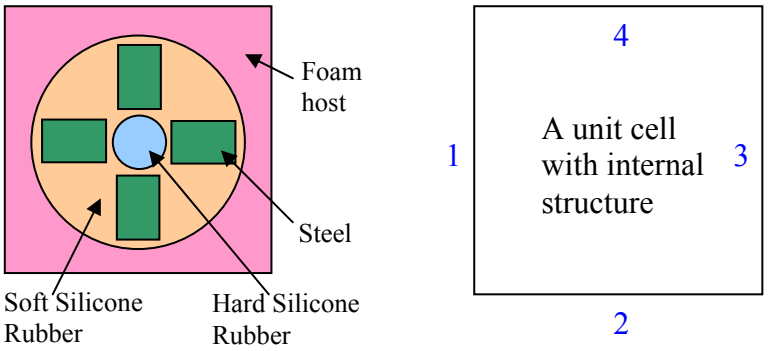

Fig. S1. A square unit cell with 4 boundaries, i.e. 1,2,3,4

We introduce a way to calculate the effective medium parameters by considering the "boundary responses" of the metamaterial unit cell (boundaries should be all chosen in the host material). We consider the unit cell as the basic element unit that "feels" and "responds to" the stimulations exerted by the outside waves. Basically, we calculate some certain eigenstates and calculate the effective force, displacement, stress, and strain of the unit cell by using the eigenstate fields on the boundaries (1,2,3,4 in the right figure of Fig. S1). The effective mass and moduli can be further obtained by using the Newton's second law and the constitutive relations. This method normally gives a nonlocal effective medium, but for certain cases such as at low frequency here, we find the effective parameters do not depend on wave vector and only depend on frequency.

The effective mass density can be obtained from the Newton's second law, i.e.

$$\rho^{eff} = \frac{m^{eff}}{a^2} = \frac{F_x^{eff}}{\ddot{u}_x^{eff} a^2} = \frac{-F_x^{eff}}{\omega^2 u_x^{eff} a^2}, \tag{S4}$$

Here ρ^{eff} is the effective density. F_x^{eff} is the effective net force exerted on the unit cell in the x direction. u_x^{eff} is the effective displacement of the unit cell in the x direction. F_x^{eff} and u_x^{eff} can be obtained as $F_x^{eff} = \int T_{xx} dy\Big|_{x=a} - \int T_{xx} dy\Big|_{x=0} + \int T_{xy} dx\Big|_{y=a} - \int T_{xy} dx\Big|_{y=0}$ and $u_x^{eff} = \dfrac{\int u_x dy\Big|_{x=0} + \int u_x dy\Big|_{x=a}}{2a}$, respectively.

The effective moduli can be obtained from the constitutive relations, i.e.

$$\begin{aligned} T_{xx}^{eff} &= c_{11}^{eff} S_{xx}^{eff} + c_{12}^{eff} S_{yy}^{eff}, \\ T_{yy}^{eff} &= c_{12}^{eff} S_{xx}^{eff} + c_{11}^{eff} S_{yy}^{eff}, \\ T_{xy}^{eff} &= 2c_{44}^{eff} S_{xy}^{eff}, \end{aligned} \tag{S5}$$

which involves only 3 components, i.e. $c_{11}^{eff}, c_{22}^{eff}, c_{44}^{eff}$ as the effective stiffness tensors. Here T_{xx}^{eff}, T_{yy}^{eff} and T_{xy}^{eff} are the *xx*, *yy* and *xy* components of the effective stress tensor. S_{xx}^{eff}, S_{yy}^{eff} and S_{xy}^{eff} are the *xx*, *yy* and *xy* components of the effective strain tensor. The stresses can be obtained as $T_{xx}^{eff} = \frac{\int T_{xx}dy\big|_{x=0} + \int T_{xx}dy\big|_{x=a}}{2a}$, $T_{yy}^{eff} = \frac{\int T_{yy}dy\big|_{y=0} + \int T_{yy}dy\big|_{y=a}}{2a}$, $T_{xy}^{eff} = \frac{\int T_{xy}dx\big|_{y=0} + \int T_{xy}dx\big|_{y=a}}{2a}$ and $T_{yx}^{eff} = \frac{\int T_{xy}dy\big|_{x=0} + \int T_{xy}dy\big|_{x=a}}{2a}$. We note that $T_{xy}^{eff} = T_{yx}^{eff}$ is required for normal linear elastic solids with infinitesimal unit cells. But here the effective medium is based on a small but finite unit cell with unit length *a*, thus sometimes we may obtain $T_{xy}^{eff} \neq T_{yx}^{eff}$ which indicates local rotations of the unit cell. The strains can be obtained as $S_{xx}^{eff} = \frac{\int u_x dy\big|_{x=a} - \int u_x dy\big|_{x=0}}{a^2}$, $S_{yy}^{eff} = \frac{\int u_y dy\big|_{y=a} - \int u_y dy\big|_{y=0}}{a^2}$ and $S_{xy}^{eff} = \frac{\int u_x dx\big|_{y=a} - \int u_x dx\big|_{y=0} + \int u_y dy\big|_{x=a} - \int u_y dy\big|_{x=0}}{2a^2}$, which denote the deformation of the unit cell.

For simplicity, in the following we use $\kappa^{eff} = \frac{c_{11}^{eff} + c_{12}^{eff}}{2}$ and $\mu^{eff} = \frac{c_{11}^{eff} - c_{12}^{eff}}{2}$ instead of c_{11}^{eff} and c_{12}^{eff}. This is also because that κ^{eff} and μ^{eff} can be related to monopolar and quadrupolar local resonances in physics, respectively. Thus, our parameter set becomes $\{\rho^{eff}, \kappa^{eff}, \mu^{eff}, c_{44}^{eff}\}$. The obtained parameters for the higher negative band are plotted in Fig. S2.

DOI: 10.1038/NMAT3043

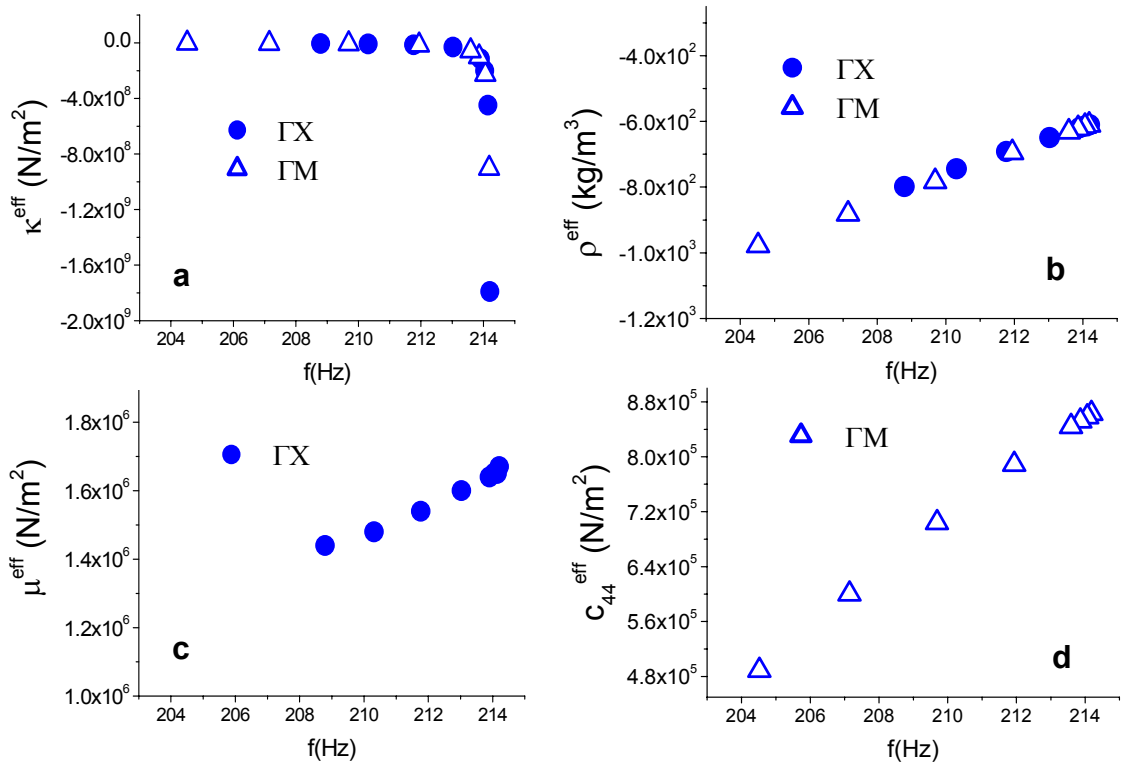

Fig. S2. The effective parameters for the higher negative band obtained by using the eigenstates along the ΓX (solid circle) or the ΓM (hollow triangle) directions. **a**. κ^{eff} **b**. ρ^{eff} **c**. μ^{eff} **d** c_{44}^{eff}. Note that μ^{eff} along the ΓM direction and c_{44}^{eff} along the ΓX direction cannot be obtained due to the eigenstate symmetries.

From the obtained effective medium parameters, we can observe the following results:

First, we note that the effective parameters are all almost real (i.e. the imaginary parts are two orders of magnitude smaller than the real parts), indicating that they are physical.

Second, these effective parameters can explain the polarizations (i.e. transverse or longitudinal) of the propagating waves in both negative bands, as have been discussed in the paper.

Third, in Fig. 2b in the paper, which plots the κ^{eff} for the higher band, we note that the data points independently obtained in ΓX and ΓM directions coincide with each other quite well, as they all lie on a smooth curve. So is μ^{eff} for the lower band plotted in Fig. 2c in the paper and ρ^{eff} in Fig. S2b here. These indicate that μ^{eff}, κ^{eff} and ρ^{eff} are the same for all eigenstates with different propagation directions at a single frequency.

Fourth, the obtained v_l^{eff} and v_t^{eff} coincide well with v_l and v_t obtained from the band structure. We have recalculated the band dispersions by using the obtained effective parameters, as have been shown as the crosses in Fig. 2a in the paper. It should be noted

that mass density should be an anisotropic tensor in general (Refs. *S2, S3*). We do find some small anisotropy in the lower band. This anisotropy has been taken into account in the calculation of v_l^{eff} and v_t^{eff}.

3. The equal-frequency surface and slowness curve contour maps of the two negative bands

Here we plot the equal-frequency surface as well as the slowness curve, which is the inverse of phase velocity, in contour maps in Fig. S3 as complimentary information to the transmission spectrum of Figure 4.

As can be seen, in the equal-frequency surfaces, both negative bands are quite isotropic near the Brillouin Zone center. But they differ significantly at large Bloch wave vectors, e.g. near the M point. However, the two slowness curve maps are not so different.

It should be noted that in both the lower and higher negative bands, there is only one mode. For the higher negative band, the mode is almost purely longitudinal in all directions of the Bloch k vector. For the lower negative band, the mode is purely longitudinal along the ΓX direction and purely transverse along the ΓM direction. But for other directions between the ΓX and ΓM directions, the mode is a hybrid mode of longitudinal and transverse waves. Thus it contains some longitudinal component and some transverse component and there is no way to separate one component from the other.

DOI: 10.1038/NMAT3043

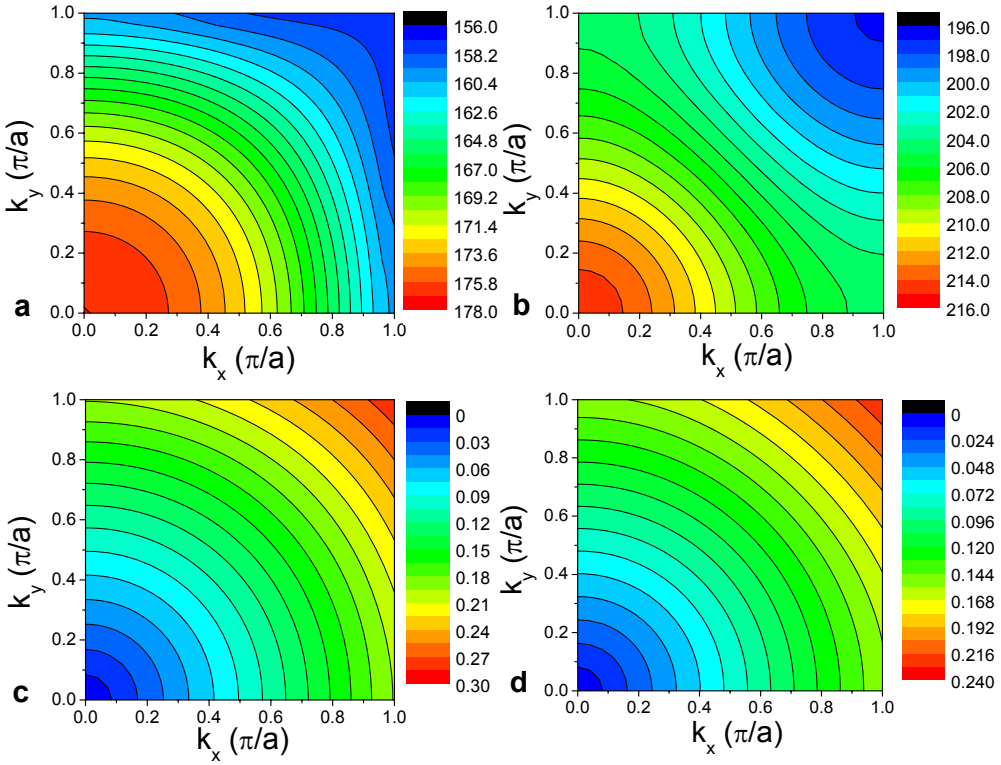

Fig. S3. The equal-frenquency surface and slowness curve contour maps. **a**. The equal-frequency surface of the lower negative band. **b**. The equal-frequency surface of the higher negative band. **c**. The slowness curve, i.e., (phase velocity)$^{-1}$, map of the lower negative band. **d**. The slowness curve map of the higher negative band.

References and Notes

S1. See e.g., Royer, D. & Dieulesaint, E., *Elastic waves in solids*, Springer, New York (1999).

S2. Milton, G. W. & Willis, J. R., On modifications of Newton's second law and linear continuum elastodynamics, *Proc. R. Soc. A* **463**, 855-880 (2007).

S3. Willis, J. R., The nonlocal influence of density variations in a composite, *Int. J. Solids Struct.* **210**, 805-817 (1985).